electronics

Article

Research on Steering-by-Wire System Motor Control Based on an Improved Sparrow Search Proportional–Integral–Derivative Algorithm

Kai Jin [1], Ping Xiao [1,2,*], Dongde Yang [3], Zhanyu Fang [1], Rongyun Zhang [1] and Aixi Yang [4,5]

[1] School of Mechanical and Automotive Engineering, Anhui Polytechnic University, Wuhu 241000, China; 2230142175@stu.aphu.edu.cn (K.J.); 2220120101@stu.aphu.edu.cn (Z.F.); hanfengzhiwei@163.com (R.Z.)
[2] Anhui Province Key Laboratory of Intelligent Car Wire-Controlled Chassis System, Anhui Polytechnic University, Wuhu 241000, China
[3] Chery Automobile Company Limited, Wuhu 241009, China; 2210120146@stu.aphu.edu.cn
[4] School of Mechanical Engineering, Zhejiang University, Hangzhou 310014, China; yangaixi@zju.edu.cn
[5] Key Laboratory Collaborat Sensing and Autonomous Unmanned System, Polytech Institute, Zhejiang University, Hangzhou 310027, China
* Correspondence: tlxp95@ahpu.edu.cn or tlxp95@163.com

Abstract: To enhance the control performance of a wire-controlled steering system, an improved sparrow search algorithm for fine-tuning the gains of a proportional–integral–derivative (SSA-PID) steering motor control algorithm is proposed. Mathematical models of the steering system and motor were derived based on an analysis of the system's structure and dynamics. A PID controller was developed with the aim of facilitating the precise control of the steering angle by targeting the angle of the steering motor. The population diversity in the sparrow algorithm was enhanced through the integration of a human learning mechanism along with a Cauchy–Gaussian variation strategy. Furthermore, an adaptive warning strategy was implemented, which employed spiral exploration to modify the ratio of early warning indicators, thereby augmenting the algorithm's capacity to evade local optima. Following these enhancements, an SSA-PID steering motor control algorithm was developed. Joint simulations were performed using the CarSim software 2019.1 and MATLAB/Simulink R2022a, and subsequent tests were conducted on a wire-controlled steering test rig. The outcomes of the simulations and bench tests demonstrate that the proposed SSA-PID regulation algorithm is capable of adapting effectively to variations and disturbances within the system, facilitating precise motor angle control and enhancing the overall reliability of the steering system.

Keywords: steering by wire; improved sparrow search algorithm; PID control; bench test; vehicle dynamics

Citation: Jin, K.; Xiao, P.; Yang, D.; Fang, Z.; Zhang, R.; Yang, A. Research on Steering-by-Wire System Motor Control Based on an Improved Sparrow Search Proportional–Integral–Derivative Algorithm. *Electronics* **2024**, *13*, 4553. https://doi.org/10.3390/electronics13224553

Academic Editor: Andrea Bonci

Received: 19 October 2024
Revised: 14 November 2024
Accepted: 18 November 2024
Published: 20 November 2024

1. Introduction

The advancement of driverless technology significantly influences the direction of future automobile development. Traditional steering systems increasingly fail to meet the electrified control requirements that are essential for automated driving. The advancement of steering-by-wire systems has been identified as a pivotal aspect in facilitating autonomous driving capabilities, as discussed in [1]. In these systems, the mechanical link between the steering wheel and the steering mechanism is replaced with an electric motor, which allows for direct operation of the steering mechanism. Therefore, precise control of the steering motor angle is considered essential [2]. However, challenges associated with the development of control algorithms for linear steering systems have impeded their widespread implementation in the automotive sector. This study presents an enhanced iteration of the sparrow search algorithm, which is renowned for its expeditious convergence, with the objective of optimizing the performance of a PID controller while striving to reduce cornering errors in the steering system.

For research on steering-by-wire systems, some scholars have adopted sliding-mode control (SMC), model predictive control (MPC), learning-based control, etc. To enhance the accuracy and robustness of the system and enable vector control of brushless DC motors in [3], an adaptive sliding-mode observer was developed to replace the velocity sensor. Control was achieved by observing the motor's induced electromotive force, eliminating the need for a velocity sensor. Due to the advantages of high power density and fast response, the comprehensive performance of permanent-magnet synchronous motors is better than that of brushless DC motors in steering system applications [4]. Reference [5] proposed a controller that combines LuGre dual observers and backstepping to respond to external disturbances and flutter using adaptive SMC. In [6], an innovative adaptive fast overtwist sliding-mode control (AFST-SMC) strategy was proposed, employing time-delay estimation (TDE) to optimize the performance of SBW systems by modifying the gain based on control errors. However, the sliding-mode variable-structure control strategy has high requirements for the nonlinearity and uncertainty of the system, and it requires a more accurate model and parameter estimation. In [7], an adaptive hierarchical control method was proposed, based on the VSR strategy of the Adaptive Network Fuzzy Inference System (ANFIS) and an integrated sliding-mode design. The proposed method was observed to accurately track both the expected yaw rate and front wheel rotation angle, thereby enhancing the stability and accuracy of the SBW system when operating in low positions. In order to make the prediction and optimization of the model more accurate, an observer and sliding-mode predictive control (DSMPC) were combined to solve the uncertainty and input constraints of a system and enhance the lateral stability [8]. In [9], model predictive control (MPC) was used to optimize the steering angle in an SBW system to improve its dynamic performance and stability. To enhance real-time control performance, researchers have investigated extreme learning machines. In the study [10], authors proposed a robust adaptive terminal sliding-mode (AITSM) control strategy that employs an extreme learning machine (ELM) to guarantee the convergence of errors and precise estimation of uncertainty. As demonstrated in [11], the ability of the sideslip angle, as well as the yaw rate, to converge was constrained, and the system exhibited a lack of robustness. To address this, the authors proposed using ARITSM for the upper controller and FNTSM for the lower controller. Simulation experiments demonstrated the effectiveness of this control scheme, achieving decoupling and optimization of the SBW system's steering performance.

PID controllers offer fast response times and high control accuracy, making them suitable for widespread use in electronic control systems. Compared to SMC, MPC, and extreme learning machines, they are particularly efficient in these aspects. The whale optimization algorithm was employed in [12] to determine the optimal PID controller parameters. The algorithm's optimization ability and convergence speed were enhanced by improving the population iteration updating method and incorporating an adaptive learning strategy. In [13–15], the BP neural network training method was integrated into the PID control strategy, resulting in enhanced performance and robustness of the regulated system. In conventional PID controllers, the control output is determined by measuring the magnitude of the system error, its rate of change, and integrating the error over time. However, PID controllers usually require the manual tuning of parameters and may not perform well for nonlinear, time-varying, or complex systems. A superior solution can be identified using the sparrow search algorithm (SSA) through a global search within the solution vector space. This makes it highly adaptable to complex nonlinear systems and multi-peak optimization problems, and the individuals in the algorithm population are adaptive and can adjust to the needs of the current environment. The sparrow algorithm facilitates the automatic adjustment of search strategies and parameter values in accordance with a problem's characteristics, thereby enhancing the robustness and stability of the PID controller. Using the sparrow algorithm for parameter optimization in a PID controller improves the system's control performance and response speed.

Various improvement strategies for addressing local optima in the SSA were summarized in [16]. A hybrid approach combining the strengths of the artificial bee colony algorithm and the SSA was proposed to improve optimization performance [17]. An improved SSA was introduced in [18], utilizing the Levy flight strategy to boost global optimization capabilities. The enhancement of population diversity was achieved in [19] through chaotic mapping combined with a greedy strategy, thereby improving the algorithm's effectiveness against local optima. In [20], a hybrid strategy was employed to augment the quality, diversity, and search capability of the preliminary population. This resulted in improved convergence accuracy and speed in specific application scenarios. The approach of chaotic mapping, as described in [21], was used to optimize both the quality and quantity of the explorer subpopulation within the SSA, thereby enhancing the global search ability of the system. In order to enhance the algorithm's capacity to circumvent local optima, a two-sample learning strategy was employed to update the follower positions. An inverse learning strategy was utilized in [22] to enhance individual exploration abilities, along with improvements to the flexible strain mechanism via a perturbation operator, adaptive weight factor, and sine–cosine factor. Additionally, a penalty processing mechanism was developed for vigilantes to ensure appropriate search solutions for individuals outside the boundary, thus guaranteeing the full utilization of each sparrow's value. However, while enhancing the algorithm's ability to search for optimal solutions, more arithmetic power and more accurate test functions are needed to meet the algorithm's operational requirements.

To address the issues mentioned above, this study introduces a steering-by-wire motor control method that uses an enhanced SSA-PID algorithm. A novel adaptive early warning strategy based on spiral exploration is proposed with the objective of enhancing the sparrow algorithm's capability to escape local optima. This is achieved by incorporating the human learning mechanism and the Cauchy–Gaussian mutation strategy, which increases population diversity in the algorithm. Then, the SSA-PID steering motor control algorithm is designed and improved. The proportional, integral, and differential coefficients are adjusted using the improved sparrow algorithm to achieve precise control of the system. To augment the anti-interference capacity of the control system, the nonlinear characteristics of the permanent-magnet synchronous motor and the impact of permanent-magnet encapsulation are taken into account. The objective of this study was to enhance the stability of the steering-by-wire system by reducing external interference and incorporating current compensation into the motor signal input. In the initial phase of the enhanced sparrow algorithm, the discrepancy between the actual and target motor angles is utilized as the fitness value. Subsequently, an iterative optimization process is employed in order to determine the optimal PID controller parameters. Then, the output of the PID controller is used as a control signal and input to the steering motor to achieve accurate control of the rotation angle. Due to the real-time acquisition of corner information and the iterative calculation of control signals, the method has high real-time performance and can quickly respond to system changes. The PID controller can adapt to changes and disturbances in the system, making the control of the steering motor more stable and reliable. Considering that actuator wear will reduce performance over time, the experimental rig will be maintained at the end of its use to extend its service life. In order to avoid the influence of temperature, humidity, light, and other environmental factors, the entire test bench is placed in a separate room, isolating it from such factors to ensure the stability of the test environment.

The remainder of this article is structured as follows. Section 2 elucidates the structure and operational principle of the wire-controlled steering system and presents the mathematical models of both the vehicle and the steering system. In Section 3, a mixed-strategy improved SSA based on PID control is proposed for the modeling of the steering motor's PMSM, and the effect of the improved algorithm is verified and applied. In Section 4, steering pedestal experiments are conducted to test the control strategy for the steering motor and the improved algorithm. Subsequently, the results are subjected to a comparative analysis with the data obtained from the simulation. Finally, the work carried out in this study is summarized in Section 5.

2. Modeling of Steering-by-Wire Systems

2.1. Structure and Working Principle of the Steering-by-Wire System

As shown in Figure 1, the steering-by-wire system includes a steering wheel module, a steering actuator module, and an electronic control unit (ECU). During operation, signals from the steering wheel are monitored using torque and angle sensors and transmitted to the ECU via a communication bus. Vehicle status information, such as speed, is also received by the ECU. The front wheel's steering angle is calculated by the control unit based on a specified algorithm, and this angle signal is sent to the steering motor through the communication bus to initiate the steering action [23]. The ECU calculates the torque of the road-sensing motor using the return torque. This feedback is then transmitted to the driver through the steering wheel, simulating the sensation provided by a mechanical connection.

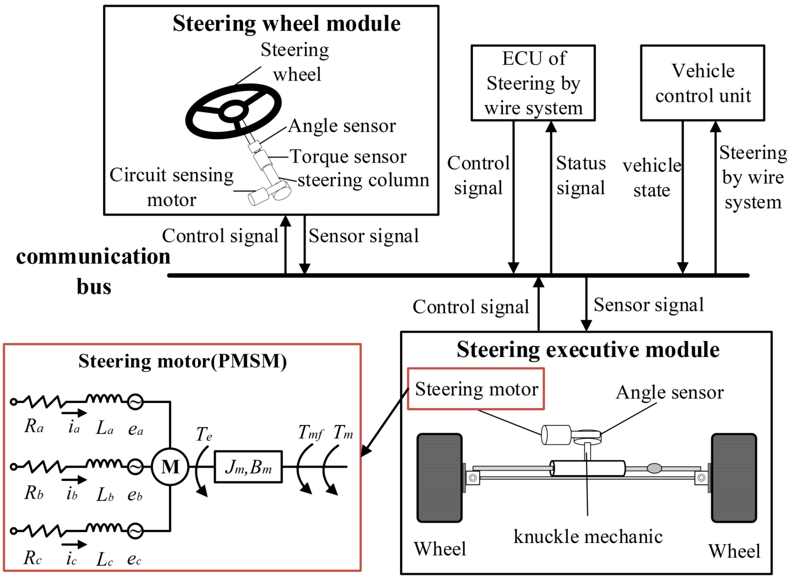

Figure 1. Schematic diagram of the structure of the steering-by-wire system.

2.2. Modeling of the Steering-by-Wire System

The steering-by-wire system consists of a steering wheel module and a steering actuation module [24]. The dynamic balance equation for the steering wheel module is derived through a detailed analysis of the steering wheel and column, as outlined below:

$$T_{sw} = J_{sw}\ddot{\theta}_{sw} + B_{\mathrm{sw}}\dot{\theta}_{sw} + K_{\mathrm{sw}}\left(\theta_{sw} - \frac{\theta_m}{G_{\mathrm{m}}}\right) + T_f \tag{1}$$

In this context, T_{sw} represents the steering wheel's input moment, J_{sw} denotes the rotational inertia of the steering wheel assembly, $B_{\mathrm{sw}} = 0.366\ \mathrm{N{\cdot}m{\cdot}s/rad}$ indicates the steering wheel's damping coefficient, and θ_{sw} refers to the steering wheel's angle. $K_{\mathrm{sw}} = 131\ \mathrm{N{\cdot}m/rad}$ is the steering wheel's torsional stiffness, θ_m is the road-sensing motor angle, $G_{\mathrm{m}} = 17$ is the road-sensing motor's reduction ratio, and T_f is the steering wheel assembly's friction moment.

The system includes a steering motor and a steering actuator. The dynamic balance equation for the steering motor is given by

$$T_M = J_M\ddot{\theta}_M + B_{\mathrm{M}}\dot{\theta}_M + K_{\mathrm{M}}\left(\theta_M - \frac{X_r}{r_{\mathrm{p}}}\right)/G_m + f_M \cdot sign\left(\dot{\theta}_M\right) \tag{2}$$

In this context, T_M denotes the output torque of the steering motor, J_M represents the motor's rotational inertia, θ_M indicates the angle of rotation of the steering motor,

$B_{\mathrm{M}} = 0.00011$ N·m·s/rad refers to the motor damping coefficient, $K_{\mathrm{M}} = 172$ N·m/rad signifies the steering motor's torsional stiffness, X_r represents the rack displacement, $r_{\mathrm{p}} = 0.00837$ mm is the radius of the pinion indexing circle, G_M denotes the steering motor's gear reduction ratio, and f_M indicates the friction within the motor and reduction mechanism.

The power balance equation for the steering motor is

$$V_M = L_M \cdot \dot{i_M} + R_{\mathrm{M}} \cdot i_M + K_{\mathrm{b}} \cdot \dot{\theta_M} \tag{3}$$

The electromagnetic torque equation is

$$T_M = \frac{P_M Z_M \phi_M i_M}{2\pi a_M} = K_M \cdot i_M \tag{4}$$

In this context, V_M represents the steering motor voltage, L_M denotes the armature inductance, i_M indicates the motor current, $R_{\mathrm{M}} = 0.44\ \Omega$ refers to the armature resistance, $K_{\mathrm{b}} = 0.072$ V·s/rad signifies the electromotive force coefficient, P_M represents the steering motor power, Z_M denotes the number of turns of the armature winding, ϕ_M is the magnetic flux per stage, and a_M indicates the number of branch circuits in the armature winding.

The equilibrium equations for the rack and pinion dynamics are

$$\begin{cases} m_{\mathrm{r}}\ddot{X}_r + B_{\mathrm{r}}\dot{X}_r + F_r = G_M T_M / r_{\mathrm{p}} \\ \theta_{sg} = X_r / r_{\mathrm{p}} \end{cases} \tag{5}$$

In this context, $m_{\mathrm{r}} = 4.21$ Kg denotes the rack mass, $B_{\mathrm{r}} = 1100$ N·m·s/rad represents the rack's damping coefficient, F_r indicates the rack's motion resistance, and θ_{sg} signifies the pinion angle.

As an example, the steering wheel's dynamic balance equation for a front-wheel-drive model is

$$J_{FW1}\theta_{FW1} + B_{\mathrm{FW1}}\theta_{FW1} = K_{\mathrm{FW1}}\left(\frac{X_r}{N_{L1}} - \theta_{FW1}\right) - T_{F1} \tag{6}$$

In this context, J_{FW1} denotes the rotational inertia of the left steering wheel, $B_{\mathrm{FW1}} = 203$ N·m·s/rad represents the damping coefficient of the left steering wheel, θ_{FW1} indicates the steering angle of the left steering wheel, $K_{\mathrm{FW1}} = 132$ N·m/rad signifies the torsional stiffness of the left steering wheel, N_{L1} represents the torsional stiffness from the rack to the left steering wheel, and T_{F1} indicates the steering resistance moment of the left steering wheel.

2.3. Simulation and Analysis of the Steering-by-Wire System

2.3.1. Variable-Ratio Design

To ensure the stability of the vehicle's handling, a method based on a constant yaw velocity gain is used to design the ideal transmission ratio [25]. This approach addresses the limitations of the constant angular velocity gain, including its poor adaptability to the dynamic system, low anti-interference capability, and mismatch with the vehicle's physical characteristics.

The two-degree-of-freedom model of the vehicle is represented as follows:

$$\begin{cases} \beta(k_1 + k_2) + \dfrac{1}{u}(ak_1 - bk_2)\omega_r - k_1\theta_{FW} = m(\dot{v} + u\omega_r) \\ \beta(ak_1 - bk_2) + \dfrac{1}{u}\left(a^2k_1 + b^2k_2\right)\omega_r - ak_1\theta_{FW} = I_z\omega_r \end{cases} \tag{7}$$

In this context, β denotes the lateral deflection angle of the vehicle's center of mass, and k_1 = 107,948.6 N/rad and k_2 = 98,538.2 N/rad represent the lateral deflection stiffnesses of the front and rear wheels, respectively. The variable u indicates the velocity component of the center of mass in the direction of vehicle motion, while $a = 1015$ mm and $b = 1895$ mm signify the distances from the front and rear axles to the center of mass, respectively. ω_r

represents the transverse angular velocity of the vehicle, $m = 1341$ Kg denotes the total mass of the vehicle, and $\theta_{FW} = (\theta_{FW1} + \theta_{FW2})/2$, with θ_{FW2} indicating the steering angle of the right steering wheel. Additionally, v represents the vertical velocity component of the center of mass, and I_z denotes the rotational moment of inertia about the z-axis.

Let K_w represent the transverse pendulum angular velocity. In the two-degree-of-freedom vehicle model, it is given by

$$\omega_r = K_\mathrm{w} \cdot \theta_{sw} = K_\mathrm{w} \cdot \theta_{FW} \cdot G = \frac{v \cdot \theta_{FW}}{1 + \frac{mv^2}{L^2}\left(\frac{a}{2k_1} - \frac{b}{2k_2}\right)} \tag{8}$$

Here, G represents the steering ratio, and $L = a + b$, $L = 2910$ mm denotes the distance between the front and rear axles of the vehicle.

Consequently, the transmission ratio G is determined as follows:

$$G = \frac{v}{K_\mathrm{w} L\left[1 + \frac{mv^2}{L^2}\left(\frac{a}{2k_1} - \frac{b}{2k_2}\right)\right]} \tag{9}$$

Since the motor turning angle is the focus of this study, the transmission ratio G_1 between the steering wheel and the steering motor must be established. For convenience, the transmission ratio G_2 between the steering motor and the wheel is set to 1.15, which is calculated using the following transmission ratio formula:

$$G = G_1 + G_2 \tag{10}$$

The transmission relationship between the steering wheel and the steering motor is given by Equation (11), where K_w is set to 0.3 s^{-1}:

$$G_1 = \frac{v}{1.15 K_\mathrm{w} L\left[1 + \frac{mv^2}{L^2}\left(\frac{a}{2k_1} - \frac{b}{2k_2}\right)\right]} \tag{11}$$

2.3.2. Simulation and Analysis of the Variable-Ratio-Based Steering Motor

In order to test the steering motor angle control effect, a variety of working conditions were set up in the CarSim software to carry out joint simulations, as shown in Figure 2.

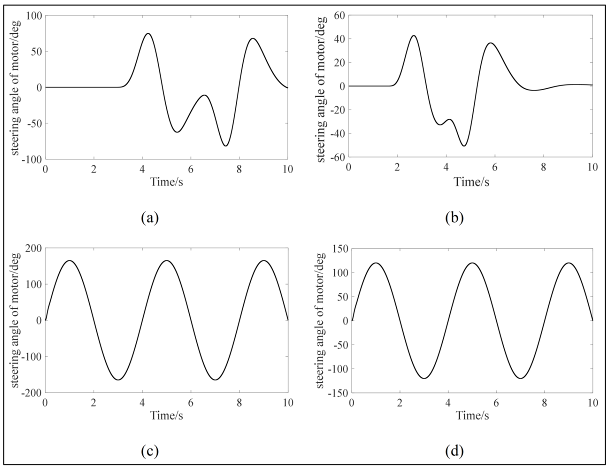

Figure 2. Steering motor angle curves under different operating conditions. (**a**) The steering motor angle curves for under 60 km/h double-shift lane-changing conditions. (**b**) The steering motor angle curves for under 90 km/h double-shift lane-changing conditions. (**c**) The steering motor angle curves for under 60 km/h sinusoidal curve conditions. (**d**) The steering motor angle curves for under 90 km/h sinusoidal curve conditions.

3. Research on the Steering Motor Control Algorithm

3.1. Steering Motor Modeling for the Steering-by-Wire System

High-precision steering control is achieved by precisely regulating the phase and amplitude of the stator current in permanent-magnet synchronous motors, which offer a higher torque density for increased output torque [26–28]. This characteristic makes permanent-magnet synchronous motors particularly well suited for steering applications that demand both high accuracy and substantial torque output. As a result, the steering motor is classified as a three-phase permanent-magnet synchronous motor.

The three-phase windings inside the motor are arranged at 120° intervals. The chain equation of the permanent-magnet synchronous motor (PMSM) in the ABC three-phase coordinate system is as follows:

$$\begin{bmatrix} \varphi_A \\ \varphi_B \\ \varphi_C \end{bmatrix} = \begin{bmatrix} L_A & M_{AB} & M_{AC} \\ M_{BA} & L_B & M_{BC} \\ M_{CA} & M_{CB} & L_C \end{bmatrix} \begin{bmatrix} i_A \\ i_B \\ i_C \end{bmatrix} + \begin{bmatrix} \varphi_f^A \\ \varphi_f^B \\ \varphi_f^C \end{bmatrix} \tag{12}$$

In this context, φ_A, φ_B, and φ_C represent the magnetic chains of the three-phase windings. L_A, L_B, and L_C denote the self-inductances of these windings, while M_{AB}, M_{AC}, M_{BA}, M_{BC}, M_{CA}, and M_{CB} indicate the mutual inductances between the three-phase windings. The currents in the windings are represented by i_A, i_B, and i_C, and φ_f^A, φ_f^B, and φ_f^C denote the magnetic chains of the three-phase windings generated by the magnetic field of the permanent magnet's excitation.

The voltage balance equation, typically employed in the context of permanent-magnet synchronous motors, is commonly written in the following form:

$$\begin{bmatrix} u_A \\ u_B \\ u_C \end{bmatrix} = \begin{bmatrix} R & 0 & 0 \\ 0 & R & 0 \\ 0 & 0 & R \end{bmatrix} \begin{bmatrix} i_A \\ i_B \\ i_C \end{bmatrix} + \begin{bmatrix} L & 0 & 0 \\ 0 & L & 0 \\ 0 & 0 & L \end{bmatrix} \frac{d}{dt} \begin{bmatrix} i_A \\ i_B \\ i_C \end{bmatrix} - \omega_r \varphi_f \begin{bmatrix} \cos\theta \\ \cos(\theta - 2\pi/3) \\ \cos(\theta + 2\pi/3) \end{bmatrix} \tag{13}$$

where u_A, u_B, and u_C are the phase voltages of the three-phase motor and R is the three-phase stator resistance.

The equation for the motor's electromagnetic torque is usually written as follows:

$$T_e = -P\varphi_f[i_A \sin\theta + i_B \sin(\theta - 2\pi/3) + i_C \sin(\theta + 2\pi/3)] \tag{14}$$

where P is the number of pole pairs of the motor rotor.

To simplify the mathematical model of the complex nonlinear system of the permanent-magnet synchronous motor (PMSM) and aid in control decoupling, a coordinate system transformation is necessary.

After applying the Clarke and Park transformations, the three-phase coordinate system undergoes a transition to become a two-phase stationary system. Subsequently, the α-β coordinates are multiplied by a rotation matrix, thereby deriving the d-q coordinate system.

The current in the d-q coordinate system is given by

$$\begin{bmatrix} i_d \\ i_q \end{bmatrix} = \begin{bmatrix} \cos\theta & \sin\theta \\ -\sin\theta & \cos\theta \end{bmatrix} \begin{bmatrix} i_\alpha \\ i_\beta \end{bmatrix} \tag{15}$$

In the d-q rotating coordinate system, i_d and i_q represent the currents, while i_α and i_β represent the currents in the α-β rotating coordinate system.

As a result of the Park transformation, the equation expressing the voltage balance is given by

$$\begin{bmatrix} u_d \\ u_q \end{bmatrix} = \begin{bmatrix} R & -\omega L_s \\ \omega L_s & R \end{bmatrix} \begin{bmatrix} i_d \\ i_q \end{bmatrix} + L\frac{d}{dt} \begin{bmatrix} i_d \\ i_q \end{bmatrix} + \begin{bmatrix} 0 \\ \omega \end{bmatrix} \tag{16}$$

In the d-q rotating coordinate system, u_d and u_q denote the voltages.

The transformed electromagnetic torque equation is

$$T_e = \frac{3}{2}P\left(\varphi_d i_q - \varphi_q i_d\right) = \frac{3}{2}P\varphi_f i_q \tag{17}$$

where φ_d and φ_q are the magnetic chains of the d and q axes, respectively.

The equation shows that the motor's electromagnetic torque can be controlled by adjusting the magnitude of the q-axis current.

3.2. *Improved SSA-PID Algorithm*

This study uses the SSA-PID control algorithm to adjust the motor angle. The parameters of PID control (K_P, K_I, and K_D) can be set by humans, and the control parameter values can be gradually changed to change the control effect. However, this method is very cumbersome, as it is not only time- and labor-consuming but also fails to reach the ideal state in terms of the control effect [29]. Using the sparrow search algorithm to determine the parameters can enhance both control stability and effectiveness. The PID controller, in conjunction with the optimization algorithm, is utilized for motor corner-tracking control, effectively enhancing the corner-following capability and steering motor accuracy. The control strategy is illustrated in Figure 3.

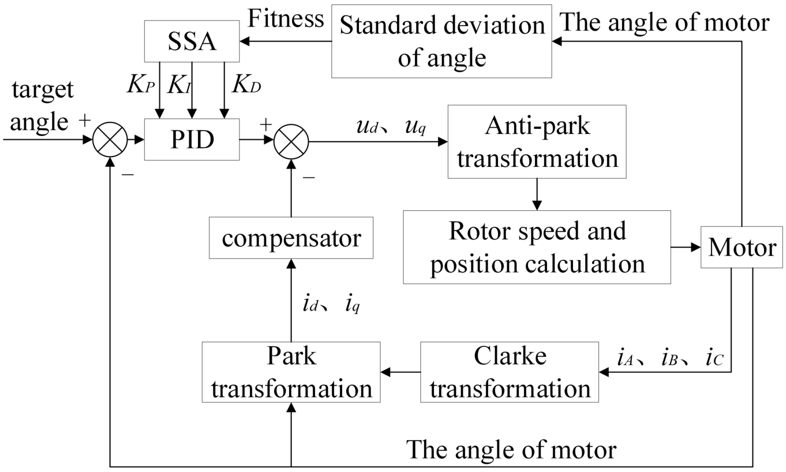

Figure 3. Block diagram of SSA-PID control algorithm.

Several improvements were proposed to the sparrow search algorithm (SSA) to improve its convergence speed and accuracy. Modifications were made to overcome the SSA's tendency to converge to local optima and enhance population diversity. A human learning mechanism was introduced to modify the update method for the individual with the worst fitness, promoting greater population diversity. Additionally, the Cauchy and Gaussian variation methods were applied to determine the step size of the variation for each individual based on its ranking position. Furthermore, the global search capability of the SSA's alarmers was enhanced through the implementation of spiral variation. To further accelerate the convergence speed, the number of alarmers was optimized using a linearly decreasing approach. The improvements are described as follows:

(1) Sparrow Algorithm Based on Human Social Learning Behavior

As the algorithm iterates, each individual in the population approaches the optimal value, resulting in a rapid decline in population diversity and a reduction in convergence accuracy [30]. To solve this problem, the idea of human social learning behavior is introduced to improve population diversity. Improvements are made to the updating method for individuals in the population through this idea. The specific improvements are detailed below.

The worst-adapted individual during each iteration, i.e., the worst individual globally, X_{worst}, is defined as follows:

$$X_{worst} = \max\{Fit(X_1), Fit(X_2), \ldots, Fit(X_M)\} \tag{18}$$

The learning factor r_3 is introduced into the position update process for population individuals to simulate human social learning behavior. This factor is defined as a random number following a standard normal distribution, N (0,1). When $r_3 > 0$, learning among the population individuals is facilitated, resulting in increased energy values and improved global optimization capabilities of the algorithm. In contrast, when $r_3 < 0$, a penalty is applied to learning, improving the algorithm's local search capability. To lessen the impact of a single parameter on the algorithm's optimal solution, two additional random learning factors, r_1 and $r2$, are introduced. These factors are defined as random numbers within the interval [0, 1] and follow a uniform distribution, with the constraint that $r_1 + r_2 = 1$. The position update formula is then revised as follows:

$$X_i^d(t+1) = X_i^d(t) + r_1\left[P_{best}^d(t) - X_i^d(t)\right] + r_2\left[G_{best}^d(t) - X_i^d(t)\right] + r_3\left[X_{worst}^d(t) - X_i^d(t)\right] \tag{19}$$

In this context, $X_i^d(t+1)$ represents the updated position of the population individuals, $X_i^d(t)$ denotes the current position, $P_{best}^d(t)$ signifies the historical optimal solution, and $G_{best}^d(t)$ indicates the global optimal solution.

(2) Cauchy–Gaussian Variation Strategy

To address the issue of sparrow individuals in the sparrow algorithm tending to experience individual assimilation in the later iterations, which leads to locally optimal solutions, a Cauchy–Gaussian mutation strategy is introduced. Following the mutation of individuals with optimal fitness using the Cauchy–Gaussian operator, a comparison of their positional energy values before and after the mutation is made. The individual exhibiting the highest positional energy value is selected for substitution in the subsequent iteration [31]. The formula is as follows:

$$X_i^d(t+1) = X_{best}^d(t) + \left[X_i^d(t) - X_k^d(t)\right] \cdot \left[\lambda_1 Cauchy\left(0, \sigma^2\right) + \lambda_2 Gauss\left(0, \sigma^2\right)\right] \tag{20}$$

In this context, X_i^d is designated as the position of the optimal-fitness individual following the mutation, X_{best}^d represents the position of the current optimal individual, and X_k^d denotes a randomly selected individual in the d-th dimension and k-th instance. The parameters λ_1 and λ_2 are updated throughout the iterations. The function $Cauchy()$ represents a random parameter that follows the Cauchy distribution, while $Gauss()$ represents a random parameter that follows the Gaussian distribution.

$$\sigma = \begin{cases} 1, f(X_{best}) < f(X_i) \\ \exp\left(\dfrac{f(X_{best}) - f(X_i)}{|f(X_{best})|}\right), otherwise. \end{cases} \tag{21}$$

(3) Adaptive Predictive Warning Based on Spiral Exploration

To address the sparrow algorithm's rapid convergence and strong optimization ability, as well as its tendency to fall into local optima, an updating strategy is proposed. This strategy enables the proportion of early-warning individuals to undergo a spiral change with respect to the number of iterations. In the first half of the algorithm's iterations, the spiral change enhances the global search capability. In the second half, the quantity of early-warning individuals is decreased using a linear-decreasing method. This approach aims to avoid local optima and improve the algorithm's convergence speed. The update process for the number of alarmers is as follows:

$$N_f = \begin{cases} int\left[z \cdot N_f^t \cdot \exp(-i/\alpha \cdot Max_{iter})\right], 0 < t \leq Max_{iter}/2 \\ N_{max} - int\left[t^2 \cdot \dfrac{N_{max} - N_{min}}{Max_{iter}}\right], Max_{iter}/2 < t \leq Max_{iter} \end{cases} \tag{22}$$

In this context, N_f represents the proportion of early warners, z denotes the spiral exploration factor, t indicates the current iteration number, α is a random number between 0 and 1, Max_{iter} is the maximum number of iterations, N_{max} is the maximum number of early warners, and N_{min} is the minimum number of early warners. The maximum number of early warners is set to 20% of the population, while the minimum number is set to 10%.

Based on the improved strategy described above, the improved hybrid sparrow search algorithm (HSSA) is proposed, and its flowchart is illustrated in Figure 4. To validate the optimization capabilities of the HSSA, both single-peak and multi-peak functions are employed to assess the convergence speed and accuracy. The functions to be tested are listed in Table 1, and the results are shown in Figure 5. Functions F1 to F3 are associated with single-peak functions, which typically contain a single global optimal solution. In contrast, functions F4 to F6 represent multi-peak functions, which are characterized by multiple locally optimal solutions. Single-peak functions are utilized to evaluate the algorithm's convergence accuracy and speed, whereas multi-peak functions are primarily used to examine the algorithm's capacity to escape local optima [32]. Figure 5a–f show the solution iteration results of the HSSA and SSA for test functions F1 to F6, respectively.

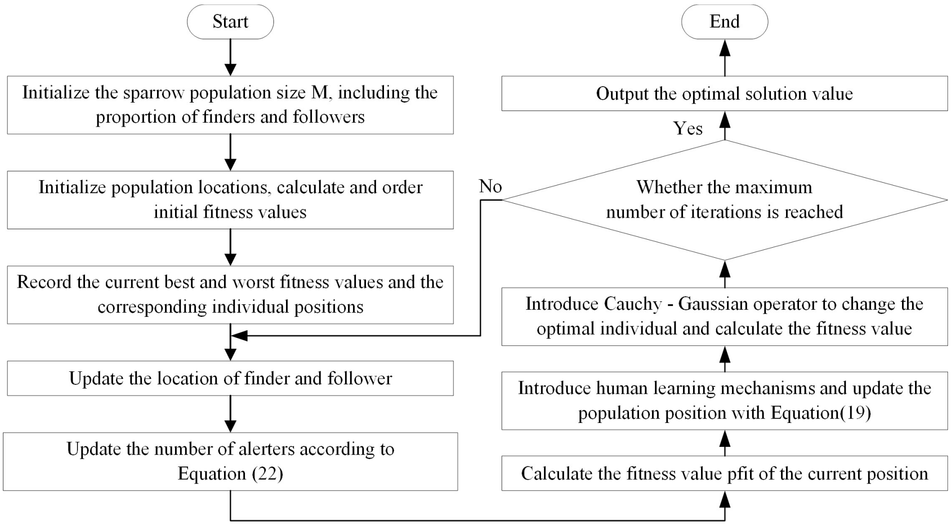

Figure 4. Flowchart illustrating the enhanced sparrow algorithm.

The convergence curves for the test functions in Figure 5 reveal that functions F1, F3, F4, and F5 display slow convergence prior to 300 iterations. This is attributed to the introduction of the Cauchy–Gaussian variation strategy, human learning mechanism, and warning mechanism of spiral exploration, all of which preserve population diversity and enhance the global exploration capability. After 300 iterations, a decrease in the number of individuals is observed, resulting in an enhanced speed of convergence and increased accuracy of the algorithm. Functions F2 and F6 are observed to reach local optima between 300 and 700 generations. The hybrid improvement strategy enhances the algorithm's ability to escape from local optima.

Table 1. Standard test functions.

Test Function	dim	Range	fmin
$F_1(x) = \sum_{i=1}^{n} x_i^2$	30	$[-100, 100]$	0
$F_2(x) = \sum_{i=1}^{n} \lvert x_i \rvert + \prod_{i=1}^{n} \lvert x_i \rvert$	30	$[-10, 10]$	0
$F_3(x) = \max\{\lvert x_i \rvert, 1 \le i \le n\}$	30	$[-100, 100]$	0
$F_4(x) = \sum_{i=1}^{n} -x_i \sin\sqrt{\lvert x_i \rvert}$	30	$[-500, 500]$	$-12{,}569.5$
$F_5(x)$	30	$[-50, 50]$	0
$y_i = 1 + (x_i + 1)/4$	30	$[-50, 50]$	0
$u(x_i, a, k, m)$	30	$[-50, 50]$	0
$F_6(x)$	30	$[-50, 50]$	0

$F_5(x)$, $u(x_i, a, k, m)$, and $F_6(x)$. See Appendix A for the specific formula.

To assess the stability of the improved algorithm, the means and standard deviations of the test results were calculated and are shown in Table 2. The standard deviation of the hybrid sparrow search algorithm (HSSA) was lower than that of the ordinary sparrow algorithm (SSA), suggesting improved stability. Furthermore, the average value was found to be closer to the optimal value, indicating an improvement in the optimization capability of the HSSA. Overall, the results demonstrate that the HSSA converges faster and achieves higher accuracy compared to the SSA.

Table 2. Comparison of the means and standard deviations of the test functions.

Test Function	SSA		HSSA	
	Average Value	Standard Deviation	Average Value	Standard Deviation
F1	3.4904×10^{-44}	1.1038×10^{-43}	3.8067×10^{-95}	1.1420×10^{-94}
F2	2.0565×10^{-47}	6.4096×10^{-47}	1.9116×10^{-53}	6.0450×10^{-53}
F3	2.2373×10^{-26}	7.0732×10^{-26}	1.0811×10^{-42}	3.4187×10^{-42}
F4	-1.0056×10^{4}	3.0748×10^{3}	-1.2561×10^{4}	2.1879×10^{1}
F5	4.5555×10^{-6}	2.2426×10^{-6}	1.3866×10^{-12}	2.9431×10^{-12}
F6	4.5700×10^{-3}	5.8466×10^{-3}	5.2126×10^{-11}	8.6025×10^{-11}

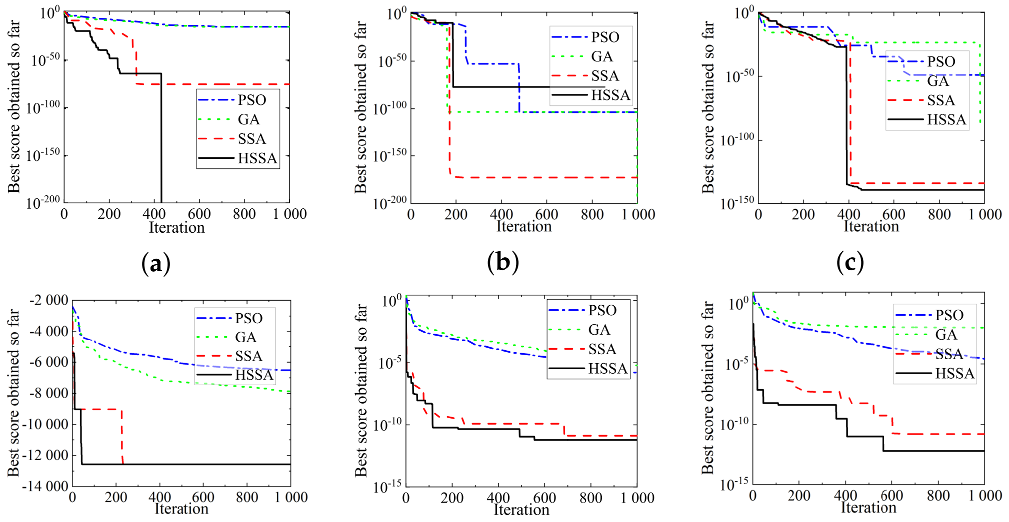

(**a**) (**b**) (**c**)

(**d**) (**e**) (**f**)

Figure 5. Comparative results of testing the optimization algorithm. (**a**) The convergence curve for the F1 test function. (**b**) The convergence curve for the F2 test function. (**c**) The convergence curve for the F3 test function. (**d**) The convergence curve for the F4 test function. (**e**) The convergence curve for the F5 test function. (**f**) The convergence curve for the F6 test function.

3.3. Simulation Analysis of the Steering Motor

The improved hybrid sparrow search algorithm (HSSA) was utilized for the parameter adjustment of PID control. The three PID parameters were defined as the population individuals in the sparrow algorithm. A target corner was defined according to the steering motor′s operating conditions. The algorithm then automatically adjusted the PID controller′s parameters based on the cornering error′s fitness value. This adjustment aimed to stabilize the actual corner of the motor near the target value.

The first step was to set the sparrow population size to 30, ensuring a broader solution space. Typically, the population size ranges from 30 to 50, with explorers making up 10% to 20% of the total. The algorithm was set to a maximum of 100 iterations. The upper and lower bounds for the initialization position (UB and LB) were determined based on the dimension of the benchmark function. To enhance search response speed, the safety value (R2) and warning value (ST) were set between 0.6 and 0.8, as shown in Table 3.

Table 3. Algorithm parameters and controller parameters.

Algorithm Parameter	Value
PID parameter range	[−100, 100]
Number of algorithm iterations	500
Population size	30
PID controller parameters	Kp = 10.283; Ki = 1.641; Kd = 0.065

Figure 6a displays the simulation results of the motor angle under double-lane-change conditions at a vehicle speed of 60 km/h, while Figure 6b shows the results at a speed of 90 km/h. Similarly, Figure 7a presents the simulation results of the motor angle under sine-wave conditions at 60 km/h, and Figure 7b illustrates the results at 90 km/h.

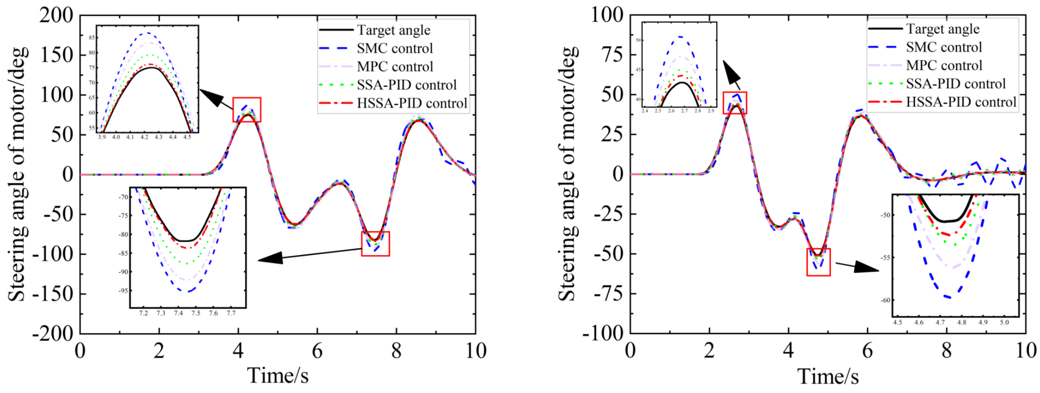

(**a**) (**b**)

Figure 6. The simulation curves of the motor angle under double-lane-change conditions. (**a**) The simulation curve of the motor angle for the double-lane-change condition at a speed of 60 km/h. (**b**) The simulation curve of the motor angle for the double-lane-change condition at a speed of 90 km/h.

Table 4 presents a summary of the simulation results for the double-lane-change conditions, displaying the mean and standard deviation of the steering motor angle deviations at vehicle velocities of 60 km/h and 90 km/h. At 60 km/h, the mean steering angle error with HSSA-PID control was 0.3582°, and the standard deviation was 0.3625, representing reductions of 74.58% and 76.02%, respectively, compared with SSA-PID control. At 90 km/h, the mean error with HSSA-PID control was 0.3516°, and the standard deviation was 0.3220, indicating decreases of 57.24% in the mean error and 53.07% in the standard deviation compared with SSA-PID control.

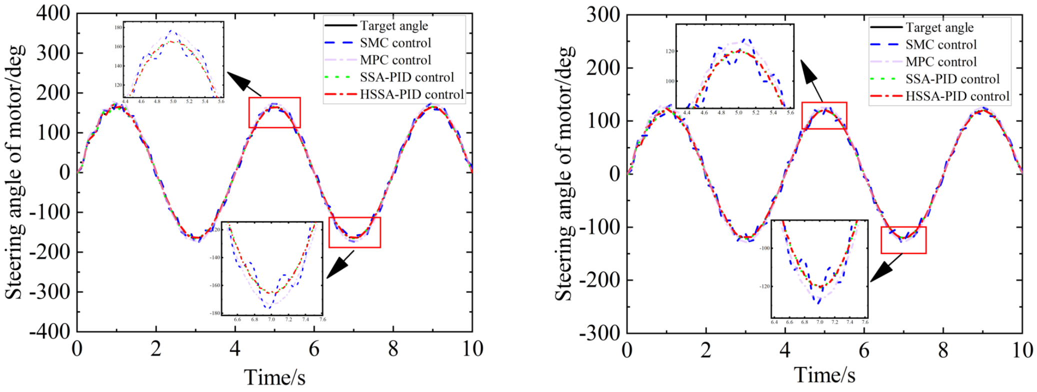

(**a**) (**b**)

Figure 7. The simulation curves of the motor angle under sine-wave conditions. (**a**) The simulation curve of the motor angle under sine-wave conditions at a speed of 60 km/h. (**b**) The simulation curve of the motor angle under sine-wave conditions at a speed of 90 km/h.

Table 4. Simulation data errors for different vehicle speeds under double-lane-change conditions. AVMSAE: average value of the motor's steering angle error; SDMSAE: standard deviation of the motor's steering angle error.

Control Strategy	**60 km/h**		**HSSA**	
	AVMSAE	**SDMSAE**	**AVMSAE**	**SDMSAE**
SMC	3.8890	4.0981	2.9424	2.4517
MPC	1.4795	1.5872	0.8634	0.7205
SSA-PID	1.4090	1.5116	0.8223	0.6862
HSSA-PID	0.3582	0.3625	0.3516	0.3220

The simulation results for the sine-wave conditions, including the mean and standard deviation of the steering motor angle errors at vehicle speeds of 60 km/h and 90 km/h, are presented in Table 5 . At 60 km/h, a mean steering angle error of 1.3505° was observed with HSSA-PID control, and the standard deviation was recorded at 2.0185°. These results indicate reductions of 8.88% in the mean error and 20.04% in the standard deviation when compared with SSA-PID control. At 90 km/h, the mean error with HSSA-PID control was observed to be 0.9567°, with a standard deviation of 1.2722°. This reflects decreases of 23.50% in the mean error and 26.83% in the standard deviation relative to SSA-PID control.

Table 5. Simulation data errors for different vehicle speeds under sinusoidal conditions.

Control Strategy	**60 km/h**		**HSSA**	
	AVMSAE	**SDMSAE**	**AVMSAE**	**SDMSAE**
SMC	7.3167	3.5783	6.2324	3.4678
MPC	1.5563	2.6507	1.3131	1.8255
SSA-PID	1.4822	2.5245	1.2506	1.7386
HSSA-PID	1.3505	2.0185	0.9567	1.2722

According to the simulation results of the step condition, the maximum overshoot of the amplitude under the control of HSSA-PID was reduced by 2.96% compared with the maximum overshoot under the control of SSA-PID. When the load was added at 0.7 s, the peak time and steady-state error under HSSA-PID control were not significantly different from those of SSA-PID, but they were improved compared with SMC and MPC.The simulation results are shown in Figure 8 and the specific data are shown in Table 6.

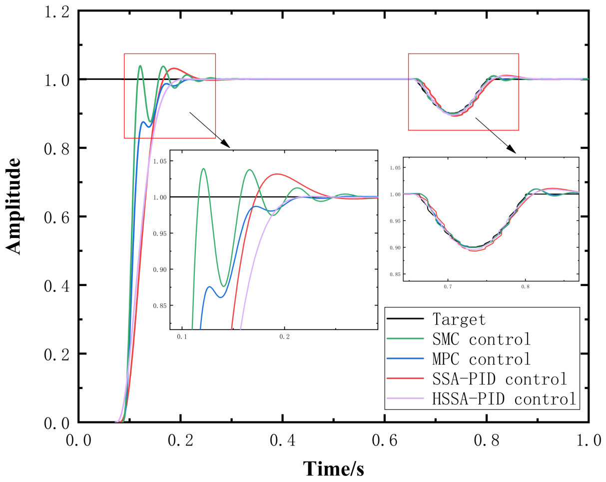

Figure 8. Step condition simulation curve.

Table 6. Comparison of simulation data under step operating conditions.

Control Strategy	0.7 s Before Maximum Overshoot	 Peak Time	0.7 s Later Steady-State Error
SMC	0.03176	0.12100	0.10695
MPC	0.00938	0.19300	0.10427
SSA-PID	0.03937	0.81400	0.10052
HSSA-PID	0.00860	0.81800	0.10048

4. Test Bench of the Steering-by-Wire System Steering Motor

4.1. Construction of Test Bench

To evaluate the reliability of the control strategy for practical applications, a test bed for the steering-by-wire system was constructed, as depicted in Figure 9. This setup included a steering wheel, a corner sensor, a steering-by-wire ECU, wheels, a rack-and-pinion steering gear, steering motors, an inferior unit, and an upper unit. The test process was as follows: first, power was supplied to the upper unit, inferior unit, steering wheel, and steering system. Then, the model built on the computer was compiled into a file type that could be recognized by the upper computer. The road conditions and operating conditions were established in the CarSim 2019.1 software, compiled, and sent to the VeriStand 20202 R4 software, where it was possible to connect the model and road condition information of the upper computer with the real-time signals of the vehicle steering system received by the inferior unit through a communication protocol, thus completing the acquisition of test data.

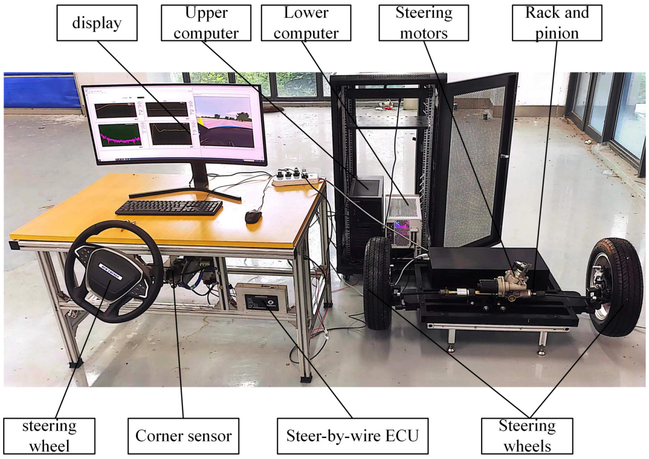

Figure 9. Test rig for the steering-by-wire system.

4.2. Test Results and Analysis

In the CarSim software, the operating conditions were initially set to 60 km/h for the double-lane-change scenario, as shown in Figure 10a. To evaluate the impact of the variable-transmission ratio, the vehicle speed was increased to 90 km/h. The results for the double-lane-change conditions are presented in Figure 10b. The test curves for the sine-wave conditions at 60 km/h and 90 km/h are shown in the subsequent Figure 11.

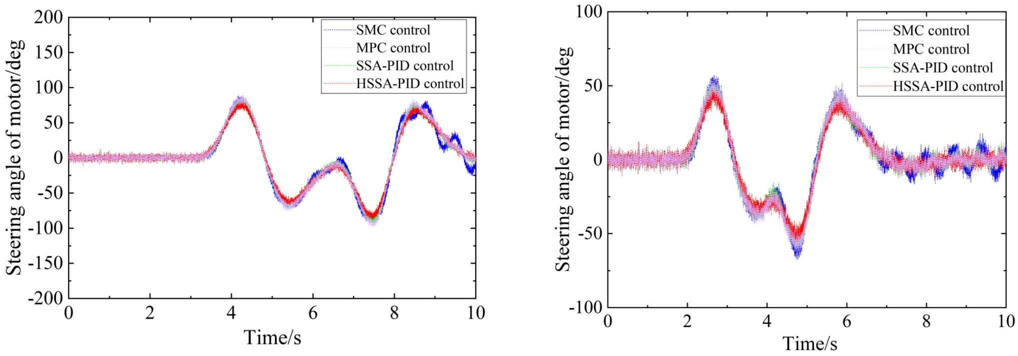

(**a**) (**b**)

Figure 10. Motor angle test curves for double-lane-change conditions. (**a**) Motor angle test curve for double-lane-change conditions at 60 km/h. (**b**) Motor angle test curve for double-lane-change conditions at 90 km/h.

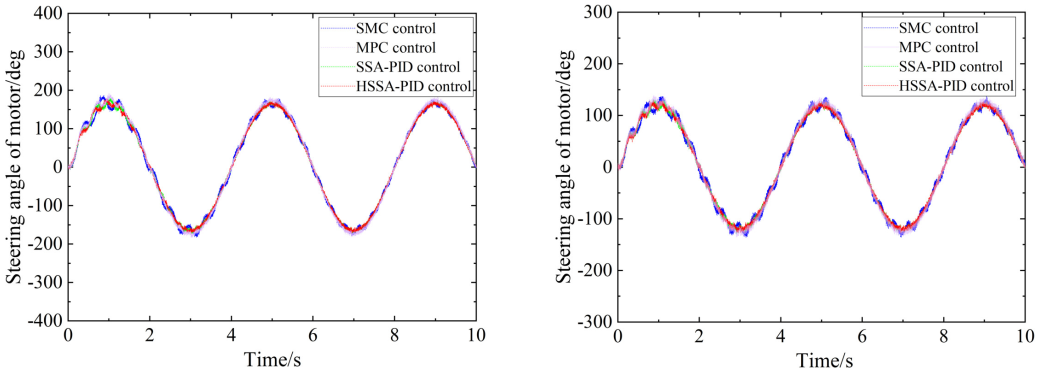

(**a**) (**b**)

Figure 11. Motor corner test curves for sine-wave conditions. (**a**) Motor corner test curve for sine-wave conditions at 60 km/h. (**b**) Motor corner test curve for sine-wave conditions at 90 km/h.

Table 7 presents the outcomes of the double-lane-change condition test, exhibiting the mean and standard deviation of steering motor angle errors at vehicle speeds of 60 km/h and 90 km/h. At a speed of 60 km/h, the mean steering angle error under HSSA-PID control was 2.5155°, with a standard deviation of 1.8930. These values reflect a 17.11% reduction in the mean error compared with SSA-PID control and an 18.18% decrease in standard deviation relative to SSA-PID control. At a speed of 90 km/h, the mean steering angle error under HSSA-PID control was 2.5343°, with a standard deviation of 1.8969, representing a 13.19% reduction in the mean error compared with SSA-PID control, along with a 14.00% decrease in the standard deviation.

Table 8 presents the simulation results under sinusoidal conditions, including both the mean value and the standard deviation of the steering motor angle errors at speeds of 60 km/h and 90 km/h. At 60 km/h, the mean steering angle error under HSSA-PID control was 2.9477°, with a standard deviation of 2.3878. These values represent an 11.25% reduction in the mean error compared with SSA-PID control and a 17.20% reduction in the standard deviation. A mean steering angle error of 2.5197° was observed for the HSSA-PID control system at a speed of 90 km/h, with a standard deviation of 1.9768. This represents a 10.94% reduction in the mean error and a 10.20% reduction in the standard deviation compared to SSA-PID control.

Table 7. Test data errors for different vehicle speeds under double-lane-change conditions.

Control Strategy	**60 km/h**		**HSSA**	
	AVMSAE	**SDMSAE**	**AVMSAE**	**SDMSAE**
SMC	5.3104	4.7104	3.9607	3.0146
MPC	3.1863	2.4291	3.0654	2.3161
SSA-PID	3.0346	2.3134	2.9194	2.2058
HSSA-PID	2.5155	1.8930	2.5343	1.8969

Table 8. Test data errors for different vehicle speeds under sinusoidal conditions.

Control Strategy	**60 km/h**		**HSSA**	
	AVMSAE	**SDMSAE**	**AVMSAE**	**SDMSAE**
SMC	7.1885	4.9050	6.4055	3.9956
MPC	3.4874	3.0282	2.9707	2.3114
SSA-PID	3.3213	2.8840	2.8292	2.2013
HSSA-PID	2.9477	2.3878	2.5197	1.9768

5. Conclusions

In view of the hardware limitations and safety problems that commercial vehicles may face when implementing the SSA-PID algorithm, this study turned to a test bench designed based on a specific model by Chery for verification. The test bench covered the key motion control aspects of the vehicle, such as steering and acceleration, and was designed to simulate the dynamic response of a vehicle under real road conditions. Through a series of experimental verifications on the bench, the feasibility of the proposed control algorithm under hardware constraints was ensured, and its influence on vehicle-handling stability and dynamic vehicle performance was evaluated. This method not only effectively avoids the risks caused by hardware and safety concerns but also provides an experimental basis for promoting the implementation of these research results in actual commercial vehicles in the future, as well as the close integration between research and applications. Following an analysis of the steering control stability issue in the steering-by-wire system, the following conclusions were reached:

(1) To enhance the steering motor′s angle control accuracy in the steer-by-wire system, an improved SSA-PID control strategy was developed. Considering that actuator wear and tear may affect performance during use, the test bench will be maintained after the end of service to extend its service life.

(2) The population diversity of the sparrow algorithm was increased by incorporating a human learning mechanism and a hybrid Cauchy–Gaussian mutation strategy. In order to enhance the exploration of the solution space and improve both the efficiency of the algorithm and its capacity to circumvent local optima, an adaptive spiral exploration method was introduced. This method updates the characteristics of the warning agents in the sparrow algorithm. As a result, a hybrid sparrow search algorithm (HSSA) was developed; it incorporated these enhancement strategies and was subsequently applied to the PID control system of the steering motor.

(3) The integration of the algorithm and the verification of its control effects were conducted on the test bench. A comparison with other control algorithms revealed that HSSA-PID control outperformed both SMC and SSA-PID control. The experimental results indicated that, under double-lane-change conditions, the mean cornering errors of steering motors controlled by HSSA-PID at speeds of 60 km/h and 90 km/h were reduced by 17.11% and 13.19%, respectively, while the standard deviations of the cornering errors were decreased by 18.18% and 14.00% compared with those of SSA-PID control. Under sine-wave conditions, the mean cornering errors were

reduced by 11.25% and 10.94%, with the standard deviations decreasing by 17.20% and 10.20%, respectively. The implementation of current compensation in the motor signal input was shown to effectively reduce external interference and the nonlinear effects within the system. This modification ensures a stable response of the steering motor to commands and enhances corner tracking control in the steer-by-wire system.

Author Contributions: Conceptualization, K.J. and P.X.; methodology, P.X.; software, K.J., D.Y., Z.F. and R.Z.; validation, P.X.; formal analysis, K.J. and D.Y.; investigation, D.Y., Z.F. and A.Y.; resources, K.J., D.Y. and Z.F.; data curation, K.J.; writing—original draft preparation, K.J.; writing—review and editing, K.J.; visualization, K.J.; supervision, P.X., R.Z. and A.Y.; project administration, K.J.; funding acquisition, P.X. All authors are in agreement with the published version of the manuscript.

Funding: In the interest of full transparency and in accordance with the norms of academic conduct, the author(s) wish to disclose the receipt of financial support in the form of grants or other forms of remuneration for the research, authorship, and publication of this article. This research is supported by the Key Research and Development Projects in Anhui Province (2022a05020007), the 2024 Anhui Provincial University Collaborative Innovation Project (GXXT-2023-039), and the National Natural Science Foundation of China (52375227).

Data Availability Statement: The original contributions presented in the study are included in the article, further inquiries can be directed to the corresponding author.

Conflicts of Interest: The author Dongde Yang was employed by the company Chery Automobile Company Limited. The remaining authors declare that the research was conducted in the absence of any commercial or financial relationships that could be construed as a potential conflict of interest.

Abbreviations

The following acronyms and abbreviations are employed throughout this manuscript:

DC	direct current
ECU	electronic control unit
HSSA	hybrid sparrow search algorithm
MPC	model predictive control
PID	proportional–integral–derivative
PMSM	permanent-magnet synchronous motor
SSA	sparrow search algorithm
SMC	sliding-mode control

Appendix A

$$F_5(x) = \frac{\pi}{n}\left\{10\sin\pi y_1 + \sum_{i=1}^{n}(yi-1)^2\left[1+10\sin^2(\pi y_{i+1})\right] + (y_n-1)^2\right\} + \sum_{i=1}^{n}u(x_i,10,100,4) \tag{A1}$$

$$u(x_i,a,k,m) = \begin{cases} k(x_i-a)^m, x_i > a \\ 0, -a < x_i < a \\ k(-x_i-a)^m, x_i < -a \end{cases} \tag{A2}$$

$$F_6(x) = 0.1\left\{\sin^2 3\pi x_1 + \sum_{i=1}^{n}(x_i-1)^2\left[1+\sin^2(3\pi x_i+1)\right] + (x_n-1)^2\left[1+\sin^2 2\pi x_n\right] + \sum_{i=1}^{n}u(x_i,5,100,4)\right\} \tag{A3}$$

References

1. Ma, B.; Wang, Y. Adaptive type-2 fuzzy sliding mode control of steer-by-wire systems with event-triggered communication. *Proc. Inst. Mech. Eng. Part D J. Automob. Eng.* **2021**, *235*, 2442–2455. [CrossRef]
2. Wang, Y.; Liu, Y.; Wang, Y.; Chai, T. Neural Output Feedback Control of Automobile Steer-by-Wire System With Predefined Performance and Composite Learning. *IEEE Trans. Veh. Technol.* **2023**, *72*, 5906-5921. [CrossRef]

3. Orman, K. Design of a memristor-based chattering free sliding mode controller and speed control of the BLDC motor. *Teh. Vjesn.* **2021**, *28*, 754–762.
4. Das, U.; Biswas, P.K. Relative study of classical and fuzzy logic controllers in a closed-loop BLDC motor drive with the GA and PSO optimization technique. *J. Appl. Res. Technol.* **2021**, *19*, 379–402. [CrossRef]
5. Liang, X.; Zhao, L.; Wang, Q.; Chen, W.; Xia, G.; Hu, J.; Jiang, P. A novel steering-by-wire system with road sense adaptive friction compensation. *Mech. Syst. Signal Process.* **2022**, *169*, 108741. [CrossRef]
6. Yang, Y.; Yan, Y.; Xu, X. Fractional Order Adaptive Fast Super-Twisting Sliding Mode Control for Steer-by-Wire Vehicles with Time-Delay Estimation. *Electronics* **2021**, *10*, 2424. [CrossRef]
7. Yang, H.; Liu, W.; Chen, L.; Yu, F. An adaptive hierarchical control approach of vehicle handling stability improvement based on Steer-by-Wire Systems. *Mechatronics* **2021**, *77*, 102583. [CrossRef]
8. Zhao, J.; Yang, K.; Cao, Y.; Liang, Z.; Li, W.; Xie, Z.; Wong, P.K. Observer-Based Discrete-Time Cascaded Control for Lateral Stabilization of Steer-by-Wire Vehicles with Uncertainties and Disturbances. *IEEE Trans. Circuits Syst.-Regul. Pap.* **2023**, *70*, 3347–3358. [CrossRef]
9. Yan, M.; Chen, W.; Wang, Q.; Zhao, L.; Liang, X.; Cai, B. Human-Machine Cooperative Control of Intelligent Vehicles for Lane Keeping-Considering Safety of the Intended Functionality. *Actuators* **2021**, *10*, 210. [CrossRef]
10. Ye, M.; Wang, H. Robust adaptive integral terminal sliding mode control for steer-by-wire systems based on extreme learning machine. *Comput. Electr. Eng.* **2020**, *86*, 106756. [CrossRef]
11. Zhang, J.; Wang, H.; Ma, M.; Yu, M.; Yazdani, A.; Chen, L. Active Front Steering-Based Electronic Stability Control for Steer-by-Wire Vehicles via Terminal Sliding Mode and Extreme Learning Machine. *IEEE Trans. Veh. Technol.* **2020**, *69*, 14713–14726. [CrossRef]
12. Mortazavizadeh, S.A.; Ghaderi, A.; Ebrahimi, M.; Hajian, M. Recent developments in the vehicle steer-by-wire system. *IEEE Trans. Transp. Electrif.* **2020**, *6*, 1226–1235. [CrossRef]
13. Mosaad, A.M.; Attia, M.A.; Abdelaziz, A.Y. Whale optimization algorithm to tune PID and PIDA controllers on AVR system. *Ain Shams Eng. J.* **2019**, *10*, 755–767. [CrossRef]
14. Pirasteh-Moghadam, M.; Saryazdi, M.G.; Loghman, E.; Kamali, A.; Bakhtiari-Nejad, F. Development of neural fractional order PID controller with emulator. *ISA Trans.* **2020**, *106*, 293–302. [CrossRef]
15. Gao, P.; Yang, P. Research on Speed Control of Three-Phase Alternating Current Asynchronous Motor Based on Back Propagation Neural Network Tuning Proportion Integration Differentiation Control. *J. Nanoelectron. Optoelectron.* **2022**, *17*, 958–966. [CrossRef]
16. Ren, L.; Zhang, W.; Ye, Y.; Li, X. Hybrid Strategy to Improve the High-Dimensional Multi-Target Sparrow Search Algorithm and Its Application. *App. Sci.* **2023**, *13*, 3589. [CrossRef]
17. Gharehchopogh, F.S. Advances in tree seed algorithm: A comprehensive survey. *Arch. Comput. Methods Eng.* **2022**, *29*, 3281–3304. [CrossRef]
18. Gad, A.G.; Sallam, K.M.; Chakrabortty, R.K.; Ryan, M.J.; Abohany, A.A. An improved binary sparrow search algorithm for feature selection in data classification. *Neural Comput. Appl.* **2022**, *34*, 15705–15752. [CrossRef]
19. Dong, J.; Dou, Z.; Si, S.; Wang, Z.; Liu, L. Optimization of capacity configuration of wind–solar–diesel–storage using improved sparrow search algorithm. *J. Electr. Eng. Technol.* **2022**, *17*, 1–14. [CrossRef]
20. Gao, B.; Shen, W.; Guan, H.; Zheng, L.; Zhang, W. Research on multistrategy improved evolutionary sparrow search algorithm and its application. *IEEE Access* **2022**, *10*, 62520–62534. [CrossRef]
21. Khedr, A.M.; Al Aghbari, Z.; Raj, P.P. MSSPP: modified sparrow search algorithm based mobile sink path planning for WSNs. *Neural Comput. Appl.* **2023**, *35*, 1363–1378. [CrossRef]
22. Tang, A.; Zhou, H.; Han, T.; Xie, L. A Chaos Sparrow Search Algorithm with Logarithmic Spiral and Adaptive Step for Engineering Problems. *Cmes-Comput. Model. Eng. Sci.* **2022**, *130*. [CrossRef]
23. Irmer, M.; Degen, R.; Nüßgen, A.; Thomas, K.; Henrichfreise, H.; Ruschitzka, M. Development and Analysis of a Detail Model for Steer-by-Wire Systems. *IEEE Access* **2023**, *11*, 7229–7236. [CrossRef]
24. He, L.; Huang, C.; Xu, Z.; Li, S.; Guo, C.; Shi, Q. A Model-Tuned Predictive Backstepping Control Approach for Angle Following of Steer-by-Wire. *IEEE Trans. Intell. Transp. Syst.* **2024**, *25*, 8053–8062. [CrossRef]
25. Shi, Q.; Wei, Y.; Xie, D.; Li, F.; Song, K.; He, L. A model predictive control approach for angle tracking of steer-by-wire system with nonlinear transmission ratio. *Asian J. Control* **2023**, *25*, 1156–1166. [CrossRef]
26. Wang, S.; Kang, J.; Degano, M.; Galassini, A.; Gerada, C. An accurate wide-speed range control method of IPMSM considering resistive voltage drop and magnetic saturation. *IEEE Trans. Ind. Electron.* **2019**, *67*, 2630–2641. [CrossRef]
27. Xu, Y.; Ding, X.; Wang, J.; Li, Y. Three-vector-based low-complexity model predictive current control with reduced steady-state current error for permanent magnet synchronous motor. *IET Electr. Power Appl.* **2020**, *14*, 305–315. [CrossRef]
28. Yi, P.; Wang, X.; Sun, Z. Interior permanent magnet synchronous motor minimum current harmonics torque ripple suppression strategy based on magnetic co-energy model. *IET Electr. Power Appl.* **2020**, *14*, 234–244. [CrossRef]
29. Zhang, J.; Zhao, C.; Guo, L. On PID control theory for nonaffine uncertain stochastic systems. *J. Syst. Sci. Complex.* **2023**, *36*, 165–186. [CrossRef]
30. Du, Y.; Yuan, H.; Jia, K.; Li, F. Research on threshold segmentation method of two-dimensional Otsu image based on improved sparrow search algorithm. *IEEE Access* **2023**, *11*, 70459–70469. [CrossRef]

31. Ding, C.; Ding, Q.; Wang, Z.; Zhou, Y. Fault diagnosis of oil-immersed transformers based on the improved sparrow search algorithm optimised support vector machine. *IET Electr. Power Appl.* **2022**, *16*, 985–995. [CrossRef]
32. Vala, T.M.; Rajput, V.N.; Geem, Z.W.; Pandya, K.S.; Vora, S.C. Revisiting the performance of evolutionary algorithms. *Expert Syst. Appl.* **2021**, *175*, 114819. [CrossRef]